frontiers | Frontiers in Energy Research

TYPE Original Research
PUBLISHED 04 August 2022
DOI 10.3389/fenrg.2022.964485

OPEN ACCESS

EDITED BY
Lianbo Ma,
Northeastern University, China

REVIEWED BY
Ming Wan,
Liaoning University, China
Tian Zhang,
Northeast Normal University, China
Haipeng Chen,
Northeast Electrical Power University, China

*CORRESPONDENCE
Xuan Fu,
fuxuan@sie.edu.cn

SPECIALTY SECTION
This article was submitted to Smart Grids,
a section of the journal
Frontiers in Energy Research

RECEIVED 08 June 2022
ACCEPTED 27 June 2022
PUBLISHED 04 August 2022

CITATION
Fu X, Wang X, Jia Q and Wang H (2022), Frequency support strategy for single-Stage grid-Connected photovoltaic generation with active power reserves. *Front. Energy Res.* 10:964485. doi: 10.3389/fenrg.2022.964485

Frequency support strategy for single-Stage grid-Connected photovoltaic generation with active power reserves

Xuan Fu[1]*, Xueying Wang[2], Qi Jia[2] and Hongjiang Wang[1]

[1]College of Information, Shenyang Institute of Engineering, Shenyang, China, [2]State Grid Liaoning Electric Power Research Institute, Shenyang, China

Large-scale photovoltaic (PV) generation grid connection causes lack of inertia and insufficient frequency regulation capacity of power system. To solve this problem, this study proposed the active power-frequency droop control (APFDC) and virtual inertia control (VIC) for single-stage PV generation. PV generation is able to participate in the grid frequency regulation by improving the control system of voltage source converter (VSC). The effect of control parameters on the inertia characteristic of PV generation is analyzed. On this basis, the distribution mechanism of unbalanced active power among PV generators with inertia control strategy is revealed. The simulation results indicated that PV generation can be controlled by setting the control strategy of the voltage source converter (VSC) to reduce or increase the active power; it also takes part in the frequency regulation of the system. The inertia provided by PV generation is controllable and frequency-dependent, increases with the increase in control gain, the decrease in the time constant of VIC, and the decrease in phase-locked loop (PLL) control bandwidth.

KEYWORDS

photovoltaic generation, frequency regulation, phase-locked loop, inertia, droop control

Introduction

The development of photovoltaic (PV) generation is an important means to deal with the current severe environmental problems and global energy transformation. At the end of 2020, the installed capacity of grid-connected PV generation in China has reached 253 million kW, indicating a year-on-year increase of 24.1%. It is estimated that by the end of 2030 and 2050, this value will reach 1,500 million and 2,700 million kW, respectively.

PV generation unit is connected to the power grid through power electronic converters. Large-scale PV generation grid connection weakens the system inertia, reduces the system ability of frequency regulation, and seriously endangers system frequency security and stability (Pedro et al., 2016; Jesus et al., 2017; Fang et al., 2019). Some countries and regions have issued requirements and technical guidelines, which require PV plants to have the ability to respond to system frequency changes (Datta

et al., 2011; Liu et al., 2014; Jibji-bukar and Anaya-lara, 2019). Field test on PV generation participating in primary frequency control was conducted by the State Grid Corporation of China (Xiaoqiang et al., 2017; Xiaoqiang et al., 2018).

A novel power point track method was proposed by Pappu et al. (2010), which is used for frequency stabilization and active power reserves. In the frequency dynamic process, the reloading algorithm is activated by the control sign; the algorithm uses a modified fractional open-circuit voltage (Mohammad et al., 2017). A power point tracking method based on Lagrange quadratic interpolation method was proposed by Yun et al. (2012) and Huanhai et al. (2013), according to the relationship of the maximum output power and output demand of PV array, related to the relationship between the maximum output power and output PV array demand, PV generation can choose between two modes (constant power output mode and MPPT mode) automatically. Zarina et al. (2014) proposed a frequency regulation method by improving the DC voltage control loop of the inverter. The method illustrates frequency regulation by establishing the proportional integral relationship between the grid frequency deviation Δf and the output DC voltage deviation ΔU_{dc}. Nevertheless, how to establish the proportional integral relationship between Δf and ΔU_{dc} is still unanswered.

In the research from "A control strategy for photovoltaic generation system based on quadratic interpolation method." (Yun et al., 2012) and "A new frequency regulation strategy for photovoltaic systems without energy storage" (Huanhai et al., 2013) and "Exploring frequency control capability of a PV system in a hybrid PV-rotating machine-without storage system." (Zarina et al., 2014), the DC voltage controller of VSC plays one of the key roles of actualizing participation in the grid frequency modulation of PV generation. The reference value of the DC capacitor voltage can be adjusted using the grid frequency deviation Δf so PV generation can participate in frequency regulation. However, it is not easy to set initial reference of the DC capacitor voltage because of the randomness of illumination and the nonlinear relationship between the DC capacitor voltage and PV array output active power. PV generation participating in frequency modulation is strictly limited by the aforementioned relationship between Δf and ΔU_{dc}. Furthermore, how to evaluate the inertia characteristics of PV generation is rarely studied.

In the study of the frequency characteristics of system with PV generation, the relationship between the output active power of PV generation and grid frequency has gained a considerable amount of attention. Therefore, a model that accurately describes the characteristics of PV generation electromechanical transient serves as the basis for on-grid analysis. At present, America's WECC and China's GB/T 32,826–2016 "Guide for modeling photovoltaic power system" have proposed a general PV generation model for electromechanical transient analysis (WECC Renewable Energy Modeling Task Force, 2012; Lei et al., 2015; SPC, 2016). (Linan et al., 2018) combined with

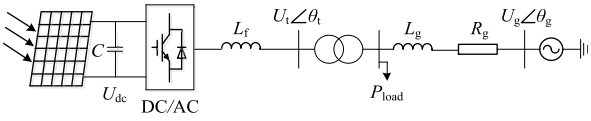

FIGURE 1
Configuration of single-stage grid-connected photovoltaic (PV) generation.

the measured data for the manual short-circuit test of a PV power station in Northwest China, effectively verified the proposed model is "verified the electromechanical transient model of PV generation." Unlike the electromagnetic transient model, the electromechanical transient model ignores numerous processes, such as PWM modulation and coordinate transformation, and replaces its DC voltage controller with active power controller (Nanou and Papathanassiou, 2014). Because of the differences between the two model control systems, there is discrepancy in designed control strategies (Sangwongwanich et al., 2017; Lyu et al., 2018).

This study proposed the virtual inertia control (VIC) strategy and the active power-frequency droop control strategy (APFDC) based on the single-stage PV generation electromechanical transient model, evaluating the inertia characteristics of PV generation. The contributions of this study are as follows:

1) The control system of VSC was improved so that PV generation actively participates in the system frequency regulation.
2) According to the relationship between unbalanced active power from the system and phase output of internal voltage, the effect of the PLL control bandwidth, control gain, and time constant on the PV generation inertia characteristics is discussed, and the effect of the PV generation inertia on frequency dynamics is analyzed.
3) The dynamic power distribution mechanism of PV generation units with VIC is revealed.

The structure of this article is arranged as follows: the configuration of single-stage grid-connected PV generation is investigated in Section 2. The electromechanical transient model of VSC is proposed in Section 3. In Section 4, the frequency regulation control strategies, including APFDC and VIC, are presented. Section 5 discusses the inertia characteristics of PV generation. The simulation results are presented in Section 6 and the conclusions in Section 7.

Configuration of single-stage grid-connected photovoltaic power generation

The structure of grid-connected single-stage PV generation is presented in Figure 1. The figure shows the main parts of the

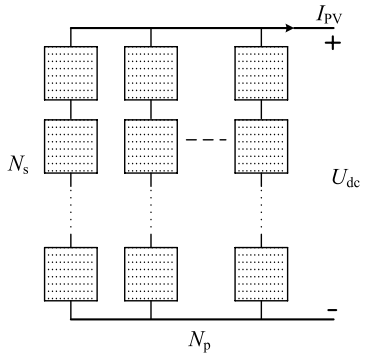

FIGURE 2
PV array model.

system, including the PV array, voltage source converter (VSC), and AC grid. The output active power of the PV array can be delivered to the grid side through the VSC (Yu et al., 2018). C is the DC filter capacitor, U_{dc} is the DC-side voltage of the PV array, L_f is the filter inductance, U_t is the voltage of point of common coupling (PCC), L_g is the inductance, R_g is the resistance of the transmission line, P_{load} is the load, and U_g is the grid side voltage.

PV array

The configuration of the PV array is presented in Figure 2, in which N_s and N_p represent the number of series and parallel connected cells. The U_{dc}-I_{PV} characteristic of a PV array from manufacturer is shown in (1).

$$I_{PV} = N_p I_{sc}\left[1 - C_1\left(e^{\frac{U_{dc}}{C_2 N_s U_{oc}}} - 1\right)\right] \tag{1}$$

Here, I_{PV} is the DC current, I_{sc} and U_{oc} are the short-circuit current and open-circuit voltage, respectively; C_1 and C_2 are coefficients obtained in (2).

$$\begin{cases} C_1 = \left(1 - \frac{I_m}{I_{sc}}\right)e^{-\frac{U_m}{C_2 U_{oc}}} \\ C_2 = \left(\frac{U_m}{U_{oc}} - 1\right)\Big/\ln\left(1 - \frac{I_m}{I_{sc}}\right) \end{cases} \tag{2}$$

Here, I_m and U_m represent the maximum current and voltage, respectively, when the PV array operates at the maximum power point.

The relationship of P_{PV} and U_{dc} is obtained in (3) based on (1).

$$P_{PV} = N_p I_{sc}\left[1 - C_1\left(e^{\frac{U_{dc}}{C_2 N_s U_{oc}}} - 1\right)\right] \cdot U_{dc} \tag{3}$$

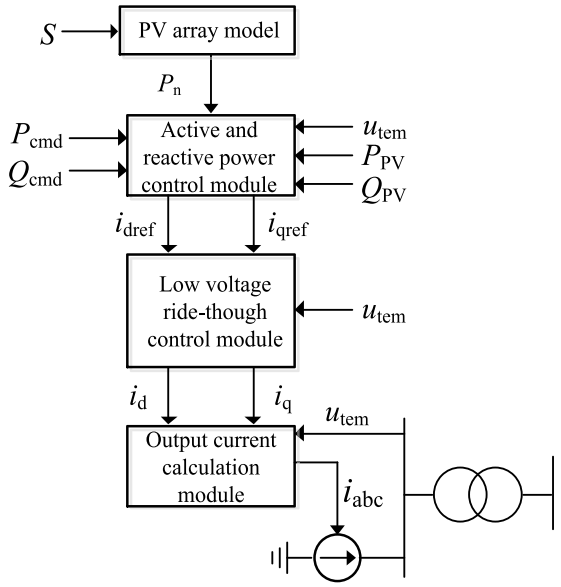

FIGURE 3
Electromechanical transient model of voltage source converter (VSC).

Simplified model of the PV array

The transcendental equation in (3) adds many difficulties to the modeling of PV array. Thus, Lei et al. (2015) proposed a simplified output active power model of PV array, which is expressed in (4).

$$P_{PV} = N_p \cdot N_s \cdot U_m \cdot I_m \cdot \frac{S}{S_{ref}}\left[1 + \frac{b}{e}(S - S_{ref})\right] \tag{4}$$

where S_{ref} is the rating irradiance, b is the constant associated with the material of battery (typical reference value b = 0.0005 m^2/W), and e is the Euler number.

The active power reserves ΔP of PV generation if operating in the limited power mode (σ% is the active power reserve ratio) is expressed in (5).

$$\Delta P = \sigma\% \cdot N_p \cdot N_s \cdot U_m \cdot I_m \cdot \frac{S}{S_{ref}}\left[1 + \frac{b}{e}(S - S_{ref})\right] \tag{5}$$

The electromechanical transient model of voltage source converter

The electromagnetic transient model of VSC is shown in Supplementary Figure SA1 of Supplementary Appendix SA, and a typical vector control strategy is shown in Supplementary Figure SA2 of Supplementary Appendix SA. In the

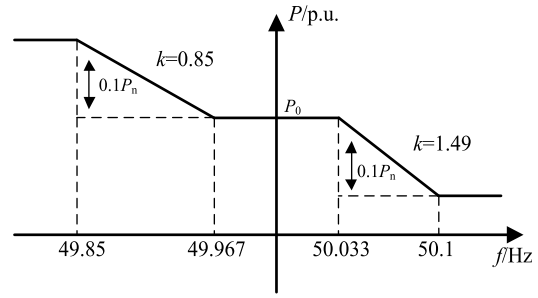

FIGURE 4
The droop characteristic curve of PV generation.

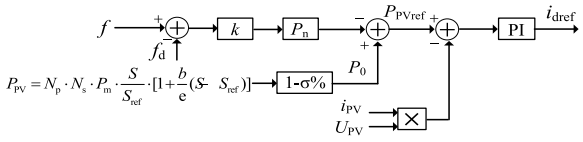

FIGURE 5
The modified control strategy of VSC.

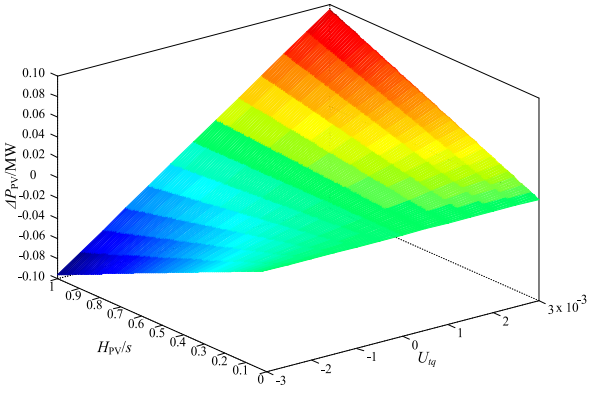

FIGURE 6
The relationship of ΔP_{PV}, H_{PV}, and U_{tq} with the fixed integral coefficient of PLL (k_{i4} = 100)

electromagnetic transient control system of VSC, it contains the current controllers, PWM modulation, etc. However, the response speed of these modules is in millisecond, and the dynamic process of rapid response can be neglected while analyzing the electromechanical transient problems.

To accurately describe the electromechanical transient characteristics of VSC, Linan et al. (2018) established an electromechanical transient model of VSC. Figure 3 shows the VSC equivalent model, where S is the illumination; P_n is the maximum active power of PV array under the current illumination; P_{cmd} and Q_{cmd} represent the reference of active and reactive powers, respectively; P_{PV} and Q_{PV} represent the actual values of active and reactive power; and u_{tem} is the PCC voltage.

Supplementary Figure SA3 of Supplementary Appendix SA shows the specific control structure of active and reactive power control modules. Compared with the electromagnetic transient control system of VSC, the active power control replaces the DC voltage control in the electromechanical transient control system of VSC; however, this part will not be described in detail. The PV generation frequency support control strategy will pay more attention to the electromechanical transient model of VSC and its control system in the next part (Varma et al., 2015; Batzelis et al., 2017).

Additional requirements

APFDC strategy

In this section, the active power-frequency droop characteristic curve of PV generation is presented in Figure 4 and the corresponding mathematical expression in (6).

$$P = P_0 - k \cdot (f - f_d) \cdot P_n \quad (6)$$

where f_d is the system frequency response value of VSC, P_n is the maximum active power output of PV generation under the current illumination, k is the frequency adjustment coefficient in 1/Hz, and P_0 is the initial output active power of PV generation.

Figure 5 shows the modified control system of VSC, where PV generation is operated under limited power mode. The output active power of PV generation (P_0) when the grid frequency f is stable is $P_{PV}^*(1-\sigma\%)$. When power disturbance occurs in the system, f is sent to the droop control loop and generates the output active power reference P_{PVref} (Firdaus and Mishra, 2019). The d-axis current reference value i_{dref} of VSC is generated by comparing the differences between P_{PVref} and P in active power controller.

VIC strategy

As can be seen from Supplementary Figure SA2 of Supplementary Appendix SA, the function of the phase-locked loop (PLL) is to align the d-axis frame with the PCC voltage $\boldsymbol{U_t}$. Supplementary Figure SA4 of Supplementary Appendix SA shows the control system of the PLL (Panda et al., 2019).

According to the control strategy of the PLL, the relationship of f and the PLL is shown in (7); (8) obtains the active power

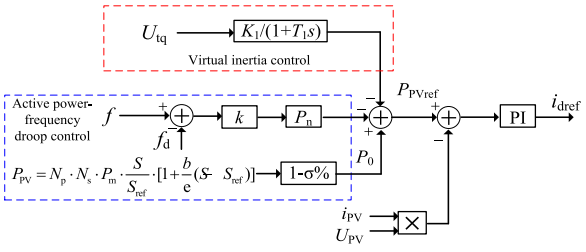

FIGURE 7
The frequency support strategy for PV generation.

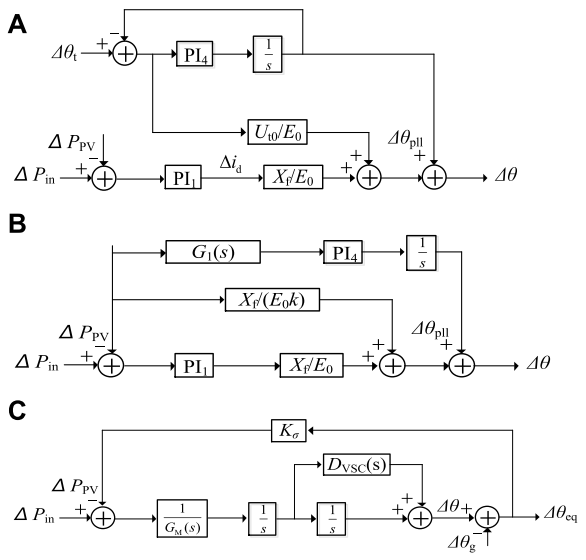

FIGURE 8
The unbalanced active power excitation–phase output response of VSC. **(A)** Block diagram of PV generation inner electric potential phase dynamic. **(B)** Block diagram of replaced PV generation voltage phase. **(C)** Block diagram of PV generation including equivalent inertia and damping coefficient.

increment ΔP_{PV} of VIC, which makes VIC based on the dynamics of PLL achieved.

$$f = \frac{U_{tq}}{2\pi} \cdot \left(k_{p4} + \int k_{i4} dt\right) \tag{7}$$

$$\Delta P_{PV} = 2H_{PV}\frac{df}{dt} = 2H_{PV} \cdot \frac{U_{tq} \cdot k_{i4}}{2\pi} \tag{8}$$

where U_{tq} is the PCC voltage in the q-axis, k_{p4} and k_{i4} are the PLL parameters, and H_{PV} is the time constant of VIC.

Figure 6 presents the relationship of ΔP_{PV}, H_{PV}, and U_{tq} with the fixed integral coefficient of PLL. Figure 6 demonstrates that as the H_{PV} and U_{tq} increase, the PV will generate more active power.

In general, APFDC and VIC are combined to participate in frequency regulation; the control strategies are shown in Figure 7. When active power disturbances occur in the system, the grid frequency disturbance f is delivered to the VIC link (a low-pass filter is introduced to the inertia control link; K_1 and T_1 are the control gain and the filter time constant, respectively), and the APFDC link can generate the power reference value because of the detection by the PLL (Anderson and Mirheydar, 1990; Ma et al., 2021a).

The inertia characteristics of photovoltaic generation

The unbalanced active power excitation–phase output response of the voltage source converter

Based on the relationship of VSC (Kakimoto et al., 2009; Fazeli et al., 2014), the inertia characteristics of PV generation with different control parameters will be further analyzed (Moradi-shahrbabak et al., 2018; Wu et al., 2018; Ma et al., 2021b). The linearization relationship of the unbalanced active power excitation–phase output response of the VSC is shown in Figure 8A (the influence of reactive power control on active power control is ignored). In Figure 8A, ΔP_{in} is the PV array output power disturbance, ΔP_{PV} is the VSC output power disturbance, $\Delta\theta_t$ is the PCC voltage phase disturbance, $\Delta\theta_{pll}$ is the PLL output phase disturbance, $\Delta\theta$ is the internal phase disturbance in VSC, and E_0 and U_{t0} are the initial of the internal voltage of VSC and the initial of PCC voltage, respectively (Yuan et al., 2017; Ma et al., 2021c).

The expression of PV generation output power and internal potential as well as the PCC voltage are presented in (9); replacing the $\Delta\theta_t$ in Figure 8A with the linearization result of (9). The relationship between the unbalanced active power excitation and the phase output response of VSC can be further simplified as in Figures 8B, C, where $G_1(s)$ is expressed in (10).

$$\begin{cases} P_{PV} = \dfrac{E \cdot U_t}{X_f}\sin(\theta - \theta_t) \\ Q_{PV} = \dfrac{E^2}{X_f} - \dfrac{E \cdot U_t}{X_f}\cos(\theta - \theta_t) \end{cases} \tag{9}$$

$$G_1(s) = \frac{X_f}{k} \cdot \left(k_{p1} + \frac{k_{i1}}{s}\right) + \frac{X_f}{U_{t0} \cdot k} \tag{10}$$

In Figure 8C, $G_M(s)$ is the equivalent inertia of PV generation, and $D_{VSC}(s)$ is the equivalent damping coefficient. $G_M(s)$ and $D_{VSC}(s)$ are related to system structure parameters and operating conditions; their expressions are presented in Supplementary Appendix SA. Furthermore, the unbalanced active power

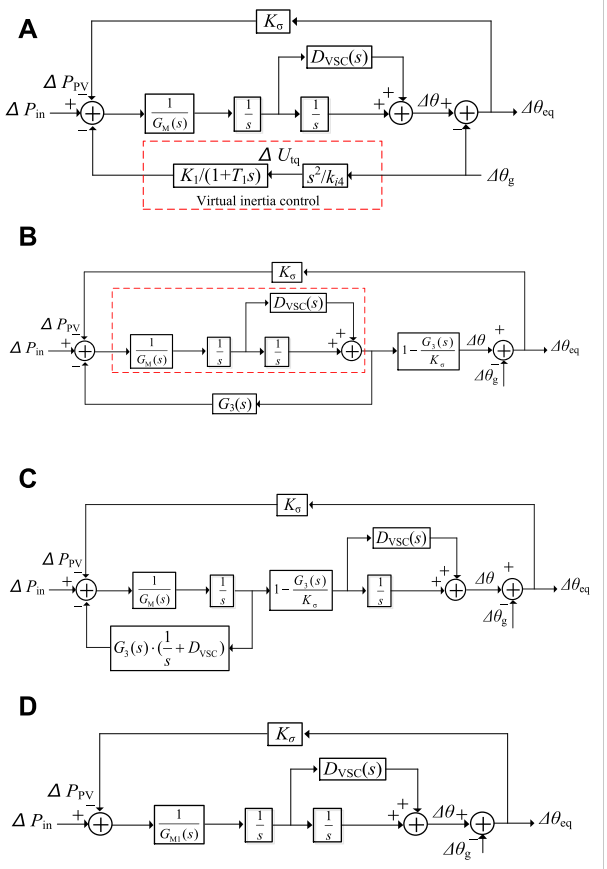

FIGURE 9
The unbalanced active power excitation–phase output response of VSC based on the virtual inertia control strategy. **(A)** Block diagram of PV generation inner electric potential phase dynamic. **(B)** Organized block diagram of PV generation inner electric potential phase dynamic. **(C)** Block diagram of input active power-output inner electric potential phase. **(D)** Block diagram of PV generation including equivalent inertia and damping coefficient.

excitation–phase output response relationship indicates how power disturbance influences the movements of E by the inertia and damping coefficient (Ma et al., 2021d) and also how coefficients are determined by the operating points and control parameters of PV generation.

Considering the relationship between the rate of range of frequency (ROCOF) and U_{tq}, the linearization result is shown in (11). When the VIC strategy is adopted in PV generation, its unbalanced active power excitation–phase output response is shown in Figure 9A and further simplified in Figures 9B, C, D.

$$\frac{d\Delta f}{dt} = \frac{\Delta U_{tq} \cdot k_{i4}}{2\pi} \tag{11}$$

In Figure 9D, its equivalent inertia $G_{M1}(s)$ is shown in (12). Based on (12), Figure 10 shows the Bode diagrams of $G_{M1}(s)$, which are obtained under different control gain coefficients K_1, different time constants T_1, and different PLL control bandwidths (Sangwongwanich et al., 2018). Figure 10shows that 1) the equivalent inertia of PV generation is frequency-dependent and controllable, different from the constant inertia of SG, and 2) with the increase in the control gain coefficient K_1 (1–30), decrease in the time constant T_1 (30–1), or decrease in the control bandwidth (9.99–3.65 Hz) of PLL, a larger inertia can be provided by PV generation in the dynamic process of grid frequency.

$$G_{M1}(s) = \frac{G_M(s) + G_3(s) \cdot \frac{1}{s} \cdot \left(\frac{1}{s} + D_{VSC}\right)}{1 - \frac{G_3(s)}{K_\sigma}} \tag{12}$$

Dynamic response analysis of grid frequency

Figure 11 shows the synchronous frequency regulation (SFR) model of SG (Linan et al., 2018). In Figure 11, T_J is the inertia time constant of SG, D_g is the equivalent damping coefficient of SG, R is the adjustment coefficient of speed regulator, T_R is the prime mover reheat time constant, F_H is the fraction of total power generated by the HP turbine, K_m is the mechanical power gain factor, P_{sp} is the incremental power set point, P_{L2} is the load power, and $\Delta\omega_g$ is the inner frequency of the internal voltage of SG.

Based on the unbalanced power excitation–phase output relation in Figure 9 and the SFR model of SG in Figure 11, it can be observed that

$$\Delta P_{in} - \Delta P_{L1} = s \cdot \Delta\omega_{PV} \cdot G_{M1}(s) \tag{13}$$

where $\Delta\omega_{PV}$ is the inner frequency of PV generation of internal voltage.

$$G_{gov}(s) = K_m \cdot \left(F_H + \frac{1 - F_H}{1 + T_R s}\right) \tag{14}$$

$$\left[\left(\Delta P_{sp} - \frac{1}{R} \cdot \Delta\omega_g\right) \cdot G_{gov}(s) - \Delta P_{L2}\right] \cdot \frac{1}{T_J s + D_g} = \Delta\omega_g \tag{15}$$

If $\Delta\omega_g = \Delta\omega_{PV}$, by combining (13) and (15), $\Delta\omega_g$ can be expressed as follows:

$$\begin{cases} -\Delta P_L = \left[\frac{1}{R} \cdot G_{gov}(s) + \left(T_J s + D_g\right) + s \cdot G_{M1}(s)\right] \cdot \Delta\omega_g \\ \Delta P_L = \Delta P_{L1} + \Delta P_{L2} \end{cases} \tag{16}$$

In this method, we give a considerable amount of attention to ΔP_L in the form of a step function, $\Delta P_L = \Delta P_s/s$. Thus,

$$\Delta\omega_g = -\frac{\frac{\Delta P_s}{s}}{\left[\frac{1}{R} \cdot G_{gov}(s) + \left(T_J s + D_g\right) + s \cdot G_{M1}(s)\right]} \tag{17}$$

According to the final value theorem, we can obtain the initial ROCOF and steady-state frequency error of the system as follows:

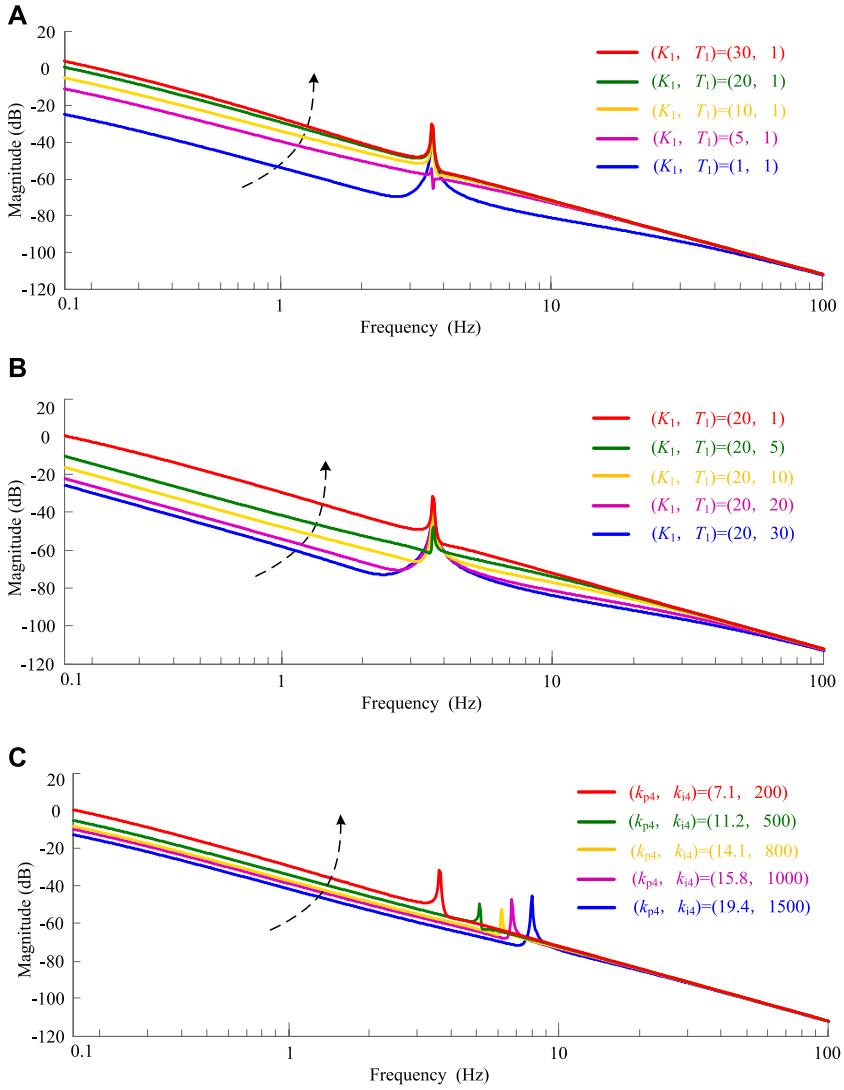

FIGURE 10
The inertia characteristics of PV generation. **(A)** Control gain coefficient variation. **(B)** Time constant variation. **(C)** PLL control bandwidths variation.

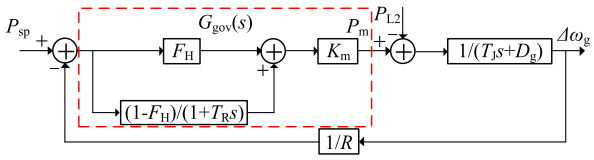

FIGURE 11
The synchronous frequency regulation (SFR) model of synchronous generator.

$$\left.\frac{d\Delta\omega_g}{dt}\right|_{t\to 0} = \lim_{s\to\infty}\left(s^2\cdot\Delta\omega_g\right) = -\frac{\Delta P_s}{T_J} \tag{18}$$

$$\left.\Delta\omega_g\right|_{t\to\infty} = \lim_{s\to 0}\left(s\cdot\Delta\omega_g\right) = -\frac{R\cdot\Delta P_s}{K_m + R\cdot D_g} \tag{19}$$

It can be seen from (17), (18), and (19) that PV generation with VIC does not affect the initial rate of change and steady-state deviation of the grid frequency (Yazdani et al., 2011; Sangwongwanich et al., 2018). However, during the dynamic of grid frequency means the dynamic characteristics of the grid frequency, PV generation plays a vital role, depending on its inertia. It can effectively restrain the drop of the lowest frequency point (or the rise of the highest frequency point) and the ROCOF under different control parameters.

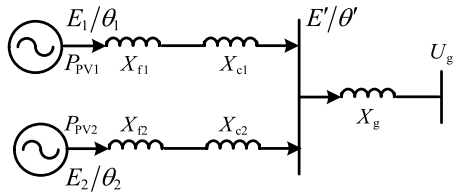

FIGURE 12
The structure of two paralleled PV generation units.

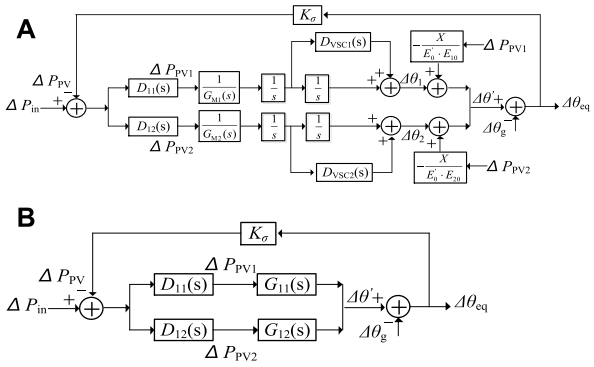

FIGURE 13
The unbalanced active power excitation–phase output response of two paralleled PV generation units based on the virtual inertia control strategy. **(A)** Block diagram of two parallel PV generation units. **(B)** Simplified block diagram of two parallel PV generation units.

The dynamic power distribution mechanism of photovoltaic generation units with the inertia control strategy

When PV generation units adopt the VIC, the dynamic power distribution mechanism of PV units is further discussed based on the unbalanced active power excitation–phase output response of VSC (Hydro Quebec TransÉnergie, 2009; Khazaei et al., 2020). The structure of two paralleled PV units is shown in Figure 12. In Figure 12, E_1 and E_2 are the magnitudes of the internal voltage vector; θ_1 and θ_2 are the phases of the internal voltage vector; E' and θ' are the magnitude and the phase of the PCC voltage vector, respectively; X_{f1} and X_{f2} are the output filter reactance; X_{c1} and X_{c2} are the reactance of each PV generation to the interconnection point; and X_g is the transmission line reactance.

The output power of each PV generation is shown in (20), linearizing (20) (neglect the effect of voltage magnitude disturbance), and the phase θ' of the PCC voltage vector can be obtained using (21).

$$\begin{cases} P_{PV1} = \dfrac{E_1 \cdot E'}{X} \sin(\theta_1 - \theta') \\ P_{PV2} = \dfrac{E_2 \cdot E'}{X} \sin(\theta_2 - \theta') \end{cases} \tag{20}$$

$$\begin{cases} \Delta\theta' = \Delta\theta_1 - \dfrac{X}{E_1 \cdot E'} \cdot \Delta P_{PV1} \\ \Delta\theta' = \Delta\theta_2 - \dfrac{X}{E_2 \cdot E'} \cdot \Delta P_{PV2} \end{cases} \tag{21}$$

where X is the total reactance.

Combining (21) and Figure 9D, the unbalanced active power excitation–phase output response of two paralleled PV generation units with the inertia control strategy is shown in Figure 13A and the simplified relationship in Figure 13B, where the derivation and expression of $G_{11}(s)$ and $G_{12}(s)$ are given in Supplementary Appendix SB; $D_{11}(s)$ and $D_{12}(s)$ are the power distribution coefficients.

According to Figure 13B, the phase θ' of the PCC voltage vector is also shown in (22), and the dynamic power distribution coefficients $D_{11}(s)$ and $D_{12}(s)$ are shown in (23) and (24).

$$\begin{cases} \Delta\theta' = D_{11}(s) \cdot G_{11}(s) \cdot \Delta P_{PV} \\ \Delta\theta' = D_{12}(s) \cdot G_{12}(s) \cdot \Delta P_{PV} \end{cases} \tag{22}$$

$$\begin{cases} D_{11}(s) = \dfrac{\dfrac{1}{G_{11}(s)}}{\dfrac{1}{G_{11}(s)} + \dfrac{1}{G_{12}(s)}} \\ D_{12}(s) = \dfrac{\dfrac{1}{G_{12}(s)}}{\dfrac{1}{G_{11}(s)} + \dfrac{1}{G_{12}(s)}} \end{cases} \tag{23}$$

$$\begin{cases} D_{11}(s) = \dfrac{G_{M1}(s)}{G_{M1}(s) + G_{M2}(s)} \\ D_{12}(s) = \dfrac{G_{M2}(s)}{G_{M1}(s) + G_{M2}(s)} \end{cases} \tag{24}$$

From (24), it can be seen that the dynamic power distribution coefficients depend on the inertia characteristics of PV generation units. Therefore, the dynamic power distribution mechanisms are similar to those of conventional synchronous generators (ENTSO-E, 2013), which is helpful in understanding the dynamic process of PV generation units with inertia control strategy.

Figure 14 presents the Bode diagrams of $D_{11}(s)$ and $D_{12}(s)$ with different control parameters. We can see from Figure 14 that with the increase in control gain, decrease in the time constant of VIC, and decrease in the PLL control bandwidth, the power distribution coefficient of PV generation in the low-frequency band will also increase, indicating that PV generation provided a more active power during active power disturbance.

Simulation validations

A simulation model was built in PSCAD/EMTDC to verify the above theory analysis, as shown in Figure 15. Table 1 presents the

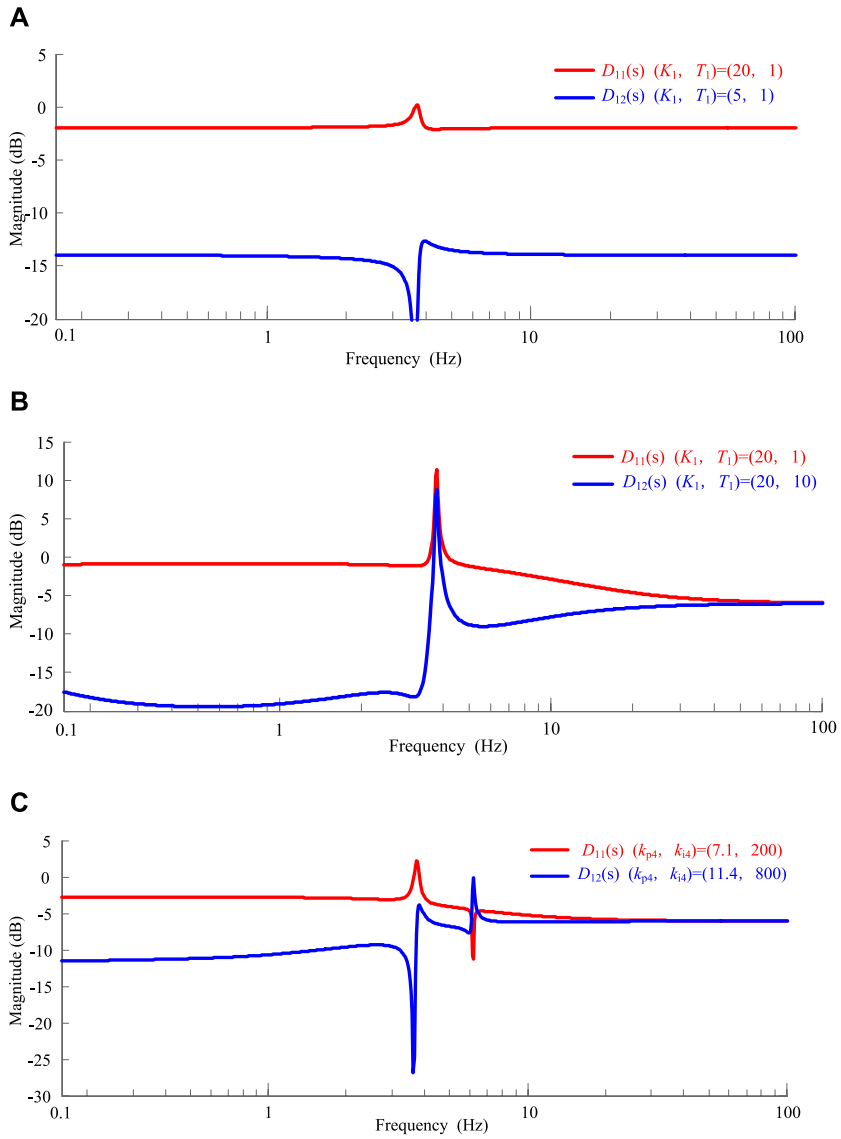

FIGURE 14
The Bode diagrams of D_{11}(s) and D_{12}(s) with different control parameters. **(A)** Control gain coefficient variation. **(B)** Time constant variation. **(C)** PLL control bandwidths variation.

main parameters of the single-stage PV system; the PV power plant is represented by a single equivalent model in the following simulations.

Photovoltaic generation responses to grid frequency disturbance simulation results

The background of the simulation is as follows: output active power of PV generation P_{PV} = 600 MW (σ% = 20%), system load P_L = 2000MW, and a load increased by 200-MW disturbance occurs at t = 40s. Figure 16 reflects the output power of synchronous unit 1 responses (P_{G1}), the output power of PV generation responses (P_{PV}) under different controls, and the grid frequency responses (f) during the disturbance.

The simulation results in Figure 16 indicated the following: 1) If PV units do not participate in the system frequency regulation, the system frequency will drop below 49.6 Hz; the ROCOF of the system is large. 2) If VIC is activated, the PV units will increase the active power by 100 MW immediately to contain the drop of frequency. However, when the system frequency tends to be stable,

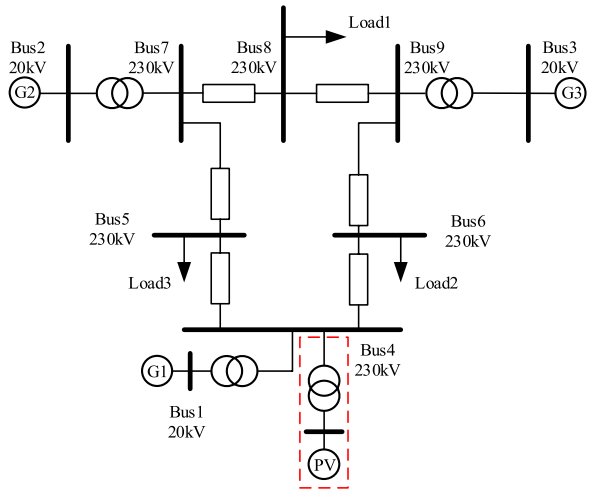

FIGURE 15
Simulation model systems.

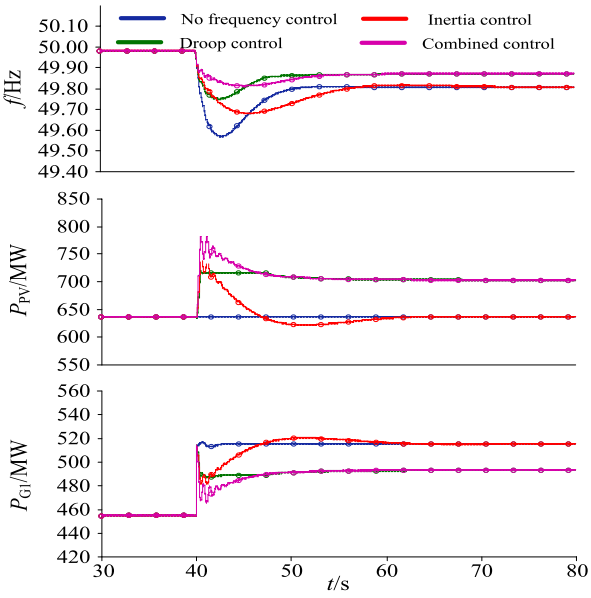

FIGURE 16
System operation curve with different control strategies.

TABLE 1 Main parameters of photovoltaic (PV) generation.

Parameters	Values
The rating power of PV array P/kW	500
The units of PV array	1,600
Active power control loop (k_{p1}, k_{i1})	(0.1, 200)
Active current control loop (k_{p2}, k_{i2})	(2, 100)
Reactive current control loop (k_{p3}, k_{i3})	(2, 100)
Phase-locked loop (k_{p4}, k_{i4})	(7.1, 200)
The control gain K_1 of a low-pass filter	20
The filter time constant T_1 of a low-pass filter	1

the PV output active power has the same value as in the first case, which means that VIC does not affect the steady-state frequency after the disturbance, only the transient-state process of system frequency. 3) If the APFDC is activated, the active power of the PV array is controlled by the VSC according to the active power-frequency droop curve shown in Figure 4. As a result, an 80-MW extra active power is added to inhibit the drop of frequency. After a dynamic process of about 20 s, the steady-state frequency of the system is about 49.85 Hz, which is higher than those in the former cases. 4) If both droop control and VIC are activated, PV generation will obviously improve the dynamic process characteristic by adding more active power. It not only increases the equivalent inertia of the system, which can constrain the ROCOF, but also reduces the frequency deviation.

The simulation results of photovoltaic generation with inertia control under different control parameters

The background of the simulation is as follows: output active power of PV generation P_{PV} = 600 MW (σ% = 20%), system load P_L = 2000 MW, and a load increased by 200-MW disturbance occurs at t = 40 s. When the low-pass filter controlled by the virtual inertia is constant (T_1 = 1 s), the control gain of the low-pass filter is increased from 5 to 20. Figure 17A indicates that with the increase in control gain, the virtual inertia of PV generation gradually increases, the ROCOF of the system during the active power disturbance decreases, and the maximum frequency deviation decreases.

When the control gain of the low-pass filter controlled by the virtual inertia is constant (K_1 = 20), T_1 is increased from 1 to 30. Figure 17B indicates that with the increase in time constant, the virtual inertia of PV generation gradually decreases, the ROCOF of the system during the active power disturbance increases, and the maximum frequency deviation increases.

Figure 17C shows the grid frequency responses at different PLL control parameters of the VSC. According to Figure 17C, with the increase in the PLL bandwidth (ω_{PLL} = 3.65–7.3 Hz), the equivalent inertia of PV generation decreases, the ROCOF of the system during the active power disturbance increases, and the maximum frequency deviation increases.

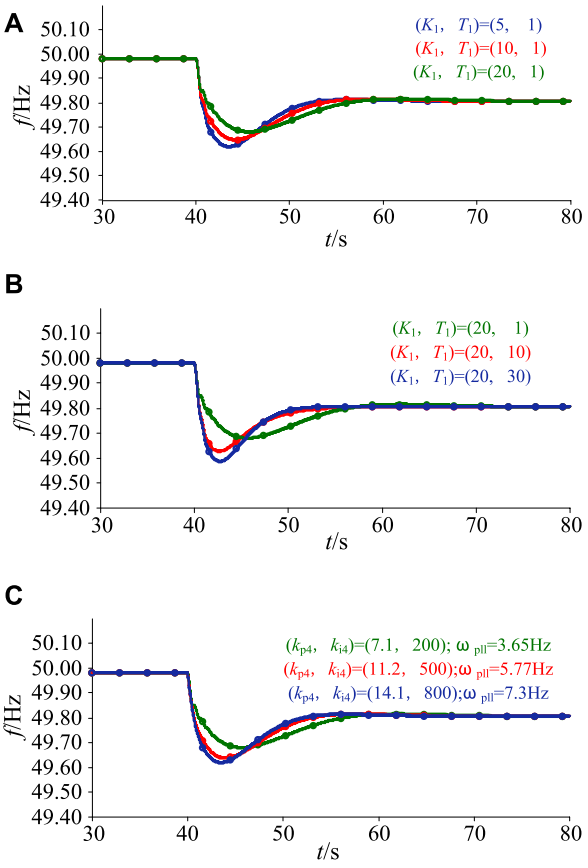

FIGURE 17
System operation curve with various control parameters. **(A)** control gain coefficient variation. **(B)** Time constant variation. **(C)** PLL control bandwidths variation.

Taken together, with the increase in control gain, more output active power can be produced in the PV generation, the ROCOF becomes smaller, and the maximum frequency deviation decreases.

Simulation result of photovoltaic power generation with inertia control under different control parameters

The PV power station consist of two PV generation units, as shown in Figure 18, the rated active output power of each PV generation unit is 400 MW (=10%), the load of the system is 2000 MW, a disturbance with 200 MW load increase occurred at t = 40 s. Figure 18 shows the active power of PV array responses (P_{in1} and P_{in2}) and the output power of PV generation unit responses (P_{PV1} and P_{PV2}) under different control parameters.

The difference between the input and output active powers of the PV array represents the unbalanced power borne by the

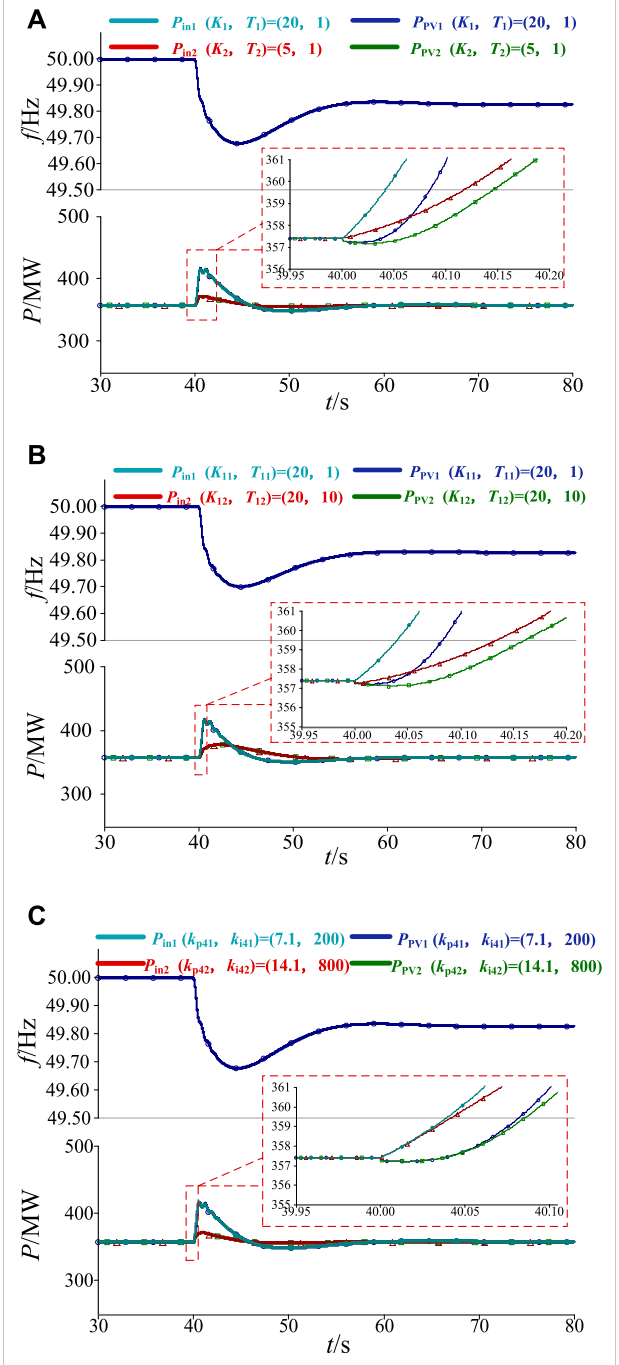

FIGURE 18
The system responses for PV generation units under different control parameters. **(A)** control gain coefficient variation. **(B)** Time constant variation. **(C)** PLL control bandwidths variation.

PV generation unit. Figure 18 shows that when the control gain K_1 of PV generation unit 1 is greater than K_2 of PV generation unit 2, the time constant T_1 is smaller than the time constant T_2, or the control bandwidth ω_{PLL1} of the PLL is

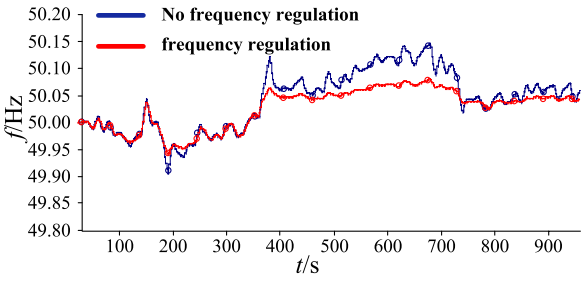

FIGURE 19
Grid frequency under the variable load.

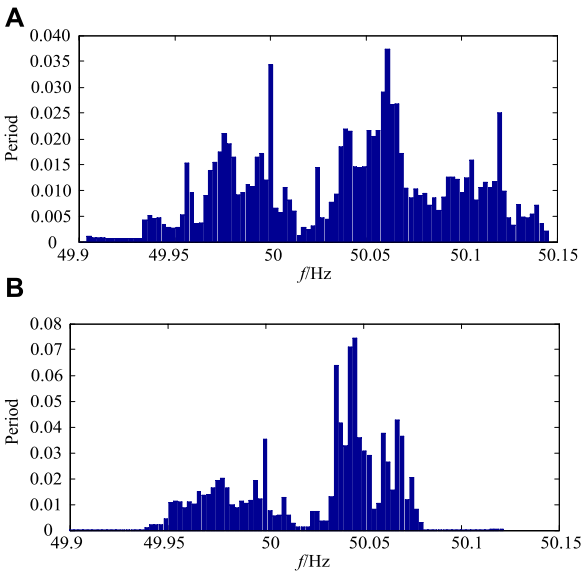

FIGURE 20
Normal distribution of grid frequency: **(A)** no frequency regulation, **(B)** frequency regulation.

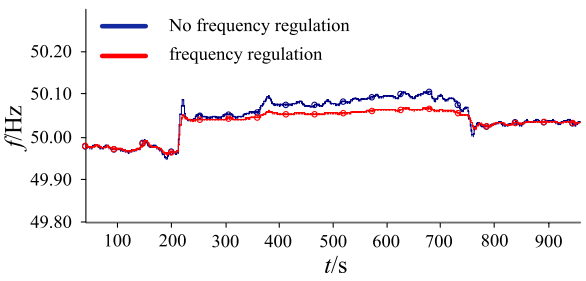

FIGURE 21
Grid frequency under variable illumination.

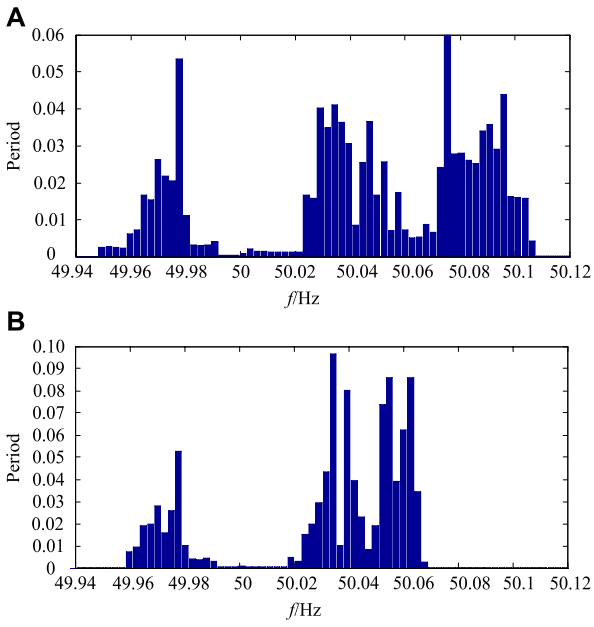

FIGURE 22
Normal distribution of grid frequency: **(A)** no frequency regulation, **(B)** frequency regulation.

smaller than ω_{PLL2}, the equivalent inertia $G_{M1}(s)$ of PV generation unit 1 is greater than $G_{M2}(s)$ of PV generation unit 2, the corresponding unbalanced power distribution coefficient $D_{11}(s)$ is greater than $D_{12}(s)$, and the unbalanced power borne by PV generation unit 1 is greater than the unbalanced power borne by PV generation unit 2 during the dynamic of grid frequency.

The simulation results of grid frequency under the variable load or irradiance

In the actual grid operation scenarios, the proposed PV generation frequency regulation strategy has proven effective. The simulation was performed under the condition of variable irradiance and load. Figure 19 presents the grid frequency responses under the variable load, and Figure 20 shows the normal distribution of grid frequency. Figure 21 presents the grid frequency responses under variable irradiance, and Figure 22 shows the normal distribution of grid frequency. We can see from Figures 19–22, we can conclude that when PV generation participates the frequency regulation, under this condition, the frequency fluctuation is inhibited as well as enhances the grid frequency stability based on the pre-set APFDC strategy and VIC strategy.

Conclusion

In this study, the single-stage PV generation frequency regulation strategies are proposed, including VIC and droop control, based on the electromechanical transient model. The method proposed in this study is to realize that the control strategies modify the VSC control system. The effect of the control parameters on the inertia characteristics is analyzed. Furthermore, the dynamic power distribution mechanism of PV generation units with the inertia control strategy is revealed, and the following conclusions were drawn:

1) The PV generation can decrease or increase the output active power controlled by VSC based on the PV generation frequency regulation strategies, thus improving the frequency stability of the system. PV generation can increase (or decrease) the output active power to respond to the changes in the system frequency when active power disturbances occur in the system according to the pre-set droop curve.
2) Different from the synchronous unit (SG), the inertia provided by PV generation with VIC is controllable and depends on the grid frequency. With the increase in the gain, decrease in the time constant of the VIC, and decrease in the control bandwidth of PLL, more inertia will be provided by PV generation.
3) The dynamic power distribution mechanisms of PV generation units with the VIC strategy are similar to those of conventional synchronous generators, which depend on the inertia characteristics of PV generation units. With the increase in the gain, decrease in the time constant of the VIC, and decrease in the control bandwidth of PLL, the active power distribution coefficient of PV generation in the low-frequency band will also increase, and thus, more active power can be provided to constrain the changes in the grid frequency.

Data availability statement

The raw data supporting the conclusion of this article will be made available by the authors, without undue reservation.

Author contributions

XF: research paper writing, research paper structure design, simulation model design. XW: research paper writing, literature review. QJ: simulation model design. HW: research paper writing.

Conflict of interest

The authors declare that the research was conducted in the absence of any commercial or financial relationships that could be construed as a potential conflict of interest.

Publisher's note

Supplementary material

The Supplementary Material for this article can be found online at: https://www.frontiersin.org/articles/10.3389/fenrg.2022.964485/full#supplementary-material

References

Anderson, P., M., and Mirheydar, M. (1990). A low-order system frequency response model. *IEEE Trans. Power Syst.* 5 (3), 720–729. doi:10.1109/59.65898

Batzelis, E. I., Kampitsis, G. E., Papathanassiou, S. A., and Member, S. (2017). Power reserves control for PV systems with real-time MPP estimation via curve fitting. *IEEE Trans. Sustain. Energy* 8 (3), 1269–1280. doi:10.1109/tste.2017.2674693

Datta, M., Member, S., Senjyu, T., Member, S., and Yona, A. (2011). A frequency-control approach by photovoltaic generator in a PV – diesel hybrid power system. *IEEE Trans. Energy Convers.* 26 (2), 559–571. doi:10.1109/tec.2010.2089688

ENTSO-E (2013). *ENTSO-E: Network code for requirements for grid connection applicable to all generators (nc rfg)*. Brussels: Entsoe.

Fang, J., Li, H., Tang, Y., and Blaabjerg, F. (2019). On the inertia of future more-electronics power systems. *IEEE J. Emerg. Sel. Top. Power Electron.* 7 (4), 2130–2146. doi:10.1109/jestpe.2018.2877766

Fazeli, M., Ekanayake, J. B., Member, S., and Holland, P. M. (2014). Exploiting PV inverters to support local voltage. *A Small-Signal Model* 29 (2), 453–462. doi:10.1109/TEC.2014.2300012

Firdaus, A., and Mishra, S. (2019). Auxiliary signal-assisted droop-based secondary frequency control of inverter- based PV microgrids for improvement in power sharing and system stability. *IET Renew. Power Gener.* 13, 2328. doi:10.1049/iet-rpg.2018.6171

Huanhai, X., Yun, L., Zhen, W., Gan, D., and Yang, T. (2013). A new frequency regulation strategy for photovoltaic systems without energy storage. *IEEE Trans. Sustain. Energy* 4 (4), 985–993. doi:10.1109/tste.2013.2261567

Hydro Quebec TransÉnergie (2009). *Transmission provider technical requirements for the connection of power plants to the hydro-Québec transmission system*. Canada: Hydro Quebec TransÉnergie, Montréal, QC.

Jesus, C., H., Pedro, G., B., and Francisco, S. (2017). Enhanced utility-scale photovoltaic units with frequency support functions and dynamic grid support for transmission systems. *IET Renew. Power Gener.* 11 (3), 361–372. doi:10.1049/iet-rpg.2016.0714

Jibji-bukar, F., and Anaya-lara, O. (2019). Frequency support from photovoltaic power plants using offline maximum power point tracking and variable droop control. *IET Renew. Power Gener.* 13, 2278. doi:10.1049/iet-rpg.2019.0211

Kakimoto, N., Takayama, S., Satoh, H., and Nakamura, K. (2009). Power modulation of photovoltaic generator for frequency control of power system. *IEEE Trans. Energy Convers.* 24 (4), 943–949. doi:10.1109/tec.2009.2026616

Khazaei, J., Tu, Z., Member, S., Liu, W., and Member, S. (2020). Small-Signal modeling and analysis of virtual inertia-based PV systems. *IEEE Trans. Energy Convers.* 35 (2), 1129–1138. doi:10.1109/TEC.2020.2973102

Lei, Z., Lingzhi, Z., Ning, C., Zhao, D., and Qu, L. (2015). Review on generic model for renewable energy generation. *Automation Electr. Power Syst.* 39 (24), 129–138. doi:10.7500/AEPS20150629010

Linan, Q., Luming, G., Lingzhi, Z., Shuanbao, N., Shuang, Z., and Sijia, B. (2018). Transient modeling of photovoltaic power plant and its test validation. *Automation Electr. Power Syst.* 42 (10), 170–175.

Liu, Y., Xin, H., Wang, Z., and Yang, T. (2014). Power control strategy for photovoltaic system based on the Newton quadratic interpolation. *IET Renew. Power Gener.* 8, 611–620. doi:10.1049/iet-rpg.2013.0067

Lyu, X., Xu, Z., Zhao, J., and Wong, K. P. (2018). Advanced frequency support strategy of photovoltaic system considering changing working conditions. *IET Gener. Transm. &amp. Distrib.* 12, 363–370. doi:10.1049/iet-gtd.2017.0700

Ma, L., Wang, X., Wang, X., Wang, L., Shi, L., Huang, M., et al. (2021a). TCDA: Truthful combinatorial double auctions for mobile edge computing in industrial internet of things. *IEEE Trans. Mob. Comput.*, 1. doi:10.1109/TMC.2021.3064314

Ma, L., Huang, M., Yang, S., Wang, R., and Wang, X. (2021c). An adaptive localized decision variable analysis approach to large-scale multiobjective and many-objective optimization. *IEEE Trans. Cybern.* PP(99), 1–13. doi:10.1109/TCYB.2020.3041212

Ma, Lianbo., Cheng, Shi, and Shi, Yuhui (2021b). Enhancing learning efficiency of brain storm optimization via orthogonal learning design. *IEEE Trans. Syst. Man. Cybern. Syst.* 51 (11), 6723–6742, Nov. doi:10.1109/tsmc.2020.2963943

Ma, Lianbo, Li, Nan, Guo, Yinan, Huang, Min, Yang, Shengxiang, Wang, Xingwei, et al. (2021d). Learning to optimize: Reference vector reinforcement learning adaption to constrained many-objective optimization of industrial copper burdening system. *IEEE Trans. Cybern.*, 1–14. doi:10.1109/TCYB.2021.3086501

Mohammad, D., Mokhlis, H., and Saad, M. (2017). Inertia response and frequency control techniques for renewable energy sources: A review. *Renew. Sustain. Energy Rev.* 69, 144–155. doi:10.1016/j.rser.2016.11.170

Moradi-shahrbabak, Z., Member, S., and Tabesh, A. (2018). Effects of front-end converter and DC-link of a utility-scale PV energy system on dynamic stability of a power system. *IEEE Trans. Ind. Electron.* 65 (1), 403–411. doi:10.1109/tie.2017.2721902

Nanou, S. I., and Papathanassiou, S. A. (2014). Modeling of a PV system with grid code compatibility. *Electr. Power Syst. Res.* 116, 301–310. doi:10.1016/j.epsr.2014.06.021

Panda, R. K., Mohapatra, A., and Srivastava, S. C. (2019). Enhancing inertia of solar photovoltaic-based microgrid through notch filter-based PLL in SRF control. *IET Renew. Power Gener.* 14, 379. doi:10.1049/iet-gtd.2018.7058

Pappu, V., Chowdhury, B., and Bhatt, R. (2010). "Implementing frequency regulation capability in a solar photovoltaic power plant," in Proceeding of North American Power Symposium Conference, Arlington, TX, USA, 26-28 September 2010 (NAPS), 1–6.

Pedro, G., B., Jesus, C., H., and Francisco, J., R. (2016). Stability assessment for transmission systems with large utility-scale photovoltaic units. *IET Renew. Power Gener.* 10 (5), 584–597. doi:10.1049/iet-rpg.2015.0331

Sangwongwanich, A., Yang, Y., Blaabjerg, F., and Sera, D. (2017). Delta power control strategy for MultistringGrid-connected PV inverters. *IEEE Trans. Industry Appl.* 53 (4), 3862–3870. doi:10.1109/TIA.2017.2681044[

Sangwongwanich, A., Member, S., and Yang, Y. (2018). Benchmarking of constant power generation strategies for single-phase grid-connected photovoltaic systems. *IEEE Trans. Industry Appl.* 54 (1), 447–457. doi:10.1109/TIA.2017.2740380

SPC (2016). *Guide for modeling photovoltaic power system: GB/T 32826-2016*. Beijing: Standards Press of China.

Varma, R. K., Member, S., Rahman, S. A., and Vanderheide, T. (2015). New control of PV solar farm as STATCOM (PV-STATCOM) for increasing grid power transmission limits during night and day. *IEEE Trans. Power Deliv.* 30 (2), 755–763. doi:10.1109/tpwrd.2014.2375216

WECC Renewable Energy Modeling Task Force (2012). *Generic solar photovoltaic system dynamic simulation model specification*.

Wu, Z., Gao, W., Gao, T., Yan, W., Zhang, H., Yan, S., et al. (2018). State-of-the-art review on frequency response of wind power plants in power systems. *J. Mod. Power Syst. Clean. Energy* 6 (1), 1–16. doi:10.1007/s40565-017-0315-y

Xiaoqiang, S., Song, C., Xin, L., Naixin, D., Yunlong, C., and Hua, L. (2018). Test method for frequency characteristics of Northwest sending-end power grid. *Power Syst. Technol.* 42 (2), 148–153.

Xiaoqiang, S., Min, G., Xin, L., Song, C., Naixin, D., Yunlong, C., et al. (2017). Actual measurement and analysis of fast frequency response capability of PV-inverters in Northwest power grid. *Power Syst. Technol.* 41 (9), 2792–2798.

Yazdani, A., Di Fazio, A. R., Ghoddami, H., Russo, M., and Kazerani, M. (2011). Modeling guidelines and a benchmark for power system simulation studies of three-phase single-stage photovoltaic systems. *IEEE Trans. Power Deliv.* 26 (2), 1247–1264. doi:10.1109/TPWRD.2010.2084599

Yu, G., Wang, Y., Li, Z., Shi, X., Song, P., Yang, W., et al. (2018). Photovoltaic virtual synchronous generator engineering application effects analysis and optimization. *Power Syst. Technol.* 42 (9), 1–8.

Yuan, H., Xiaoming, Y., and Jiabing, H. (2017). Modeling of grid-connected VSCs for power system small-signal stability analysis in DC-link voltage control timescale. *IEEE Trans. Power Syst.* 32 (5), 3981–3991. doi:10.1109/tpwrs.2017.2653939

Yun, L., Ying, K., Huanhai, X., Lu, Z., and Gan, D. (2012). A control strategy for photovoltaic generation system based on quadratic interpolation method. *Automation Electr. Power Syst.* 36 (21), 29–35. doi:10.3969/j.issn.1000-1026.2012.21.006

Zarina, P., P., Mishra, S., and Sekhar, P., C. (2014). Exploring frequency control capability of a PV system in a hybrid PV-rotating machine-without storage system. *Int. J. Electr. Power & Energy Syst.* 60, 258–267. doi:10.1016/j.ijepes.2014.02.033